Supporting Information

Closed pore structure engineering from ultra-micropore with the assistance of polypropylene for boosted sodium ion storage

Xue Li, *Ning Sun*,* *Shaohong Zhang*, *Razium Ali Soomro*, *Bin Xu**

Experimental section

Materials preparation

PVDF-derived porous carbons (PFC) were obtained by the direct carbonization of PVDF (Kynar 761, Arkema Co.) under argon flow at 800 ℃ for 1 h. For the fabrication of closed pore structure, PFC was firstly mixed with polypropylene (PP) in the ratio of 1:2 by ball milling treatment under solvent-free conditions. The resulting mixture was then subjected to pre-oxidation treatment at 330 ℃ for 1 h, and the immediate product was denoted as PFC@PP. The closed pore enriched carbon (PFCC@PP) was ultimately obtained after further carbonization at 1300 ℃ for 2 h under an argon flow. For comparison, PFC was also subjected to further carbonization at 1300 ℃ for 2 h without the addition of PP, and the resulting sample was designated as PFCC.

Materials characterization

The morphologies of the samples were obtained using a scanning electron microscope (SEM, SU8000, Hitachi, Japan) and high-resolution transmission electron microscopy (HR-TEM, Tecnai G2 F30, FEI, American). The microcrystalline structure was analyzed using x-ray diffraction (XRD, Ultima IV, Rigaku, Japan) of Cu Kα radiation (λ = 1.54056 Å) and a confocal micro-Raman spectrometer (inVia Reflex, Renishaw, England) with a laser wavelength of 633 nm. The thermal stability was investigated using a simultaneous thermal analyzer (TGA/DSC3+, METTLER, Switzerland). The evolution of functional groups was characterized using a Fourier transform infrared spectrometer (Nicolet 6700, Thermo Fisher, American). XPS

analysis was performed using an X-ray photoelectron spectrometer (ESCALAB 250, THERMO VG, American). The N_2 adsorption-desorption tests were carried out using a Micromeritics ASAP2460 analyzer. The true density of the samples was tested using the AccuPyc II 1340 analyzer with helium as the analysis gas. The Xeuss 2.0 SAXS/WAXS system was used for small angle X-ray scattering (SAXS) test to characterize the closed pores of the samples, with a Cu X-ray source of 30 W (λ = 1.542 nm Å).

Electrochemical measurements

The electrochemical performance of the carbons was tested in CR2025-type coin cells. For the preparation of working electrodes, the uniform slurry containing active material and CMC binder with a mass ratio of 95:5 was spread over the copper foil current collector. After being vacuum dried at 120 °C for 10 h and then cut into circular pieces with a diameter of 10 mm, the electrode was obtained with the average mass loading of active materials controlled about 1 mg cm^{-2}. The coin cells were assembled in an argon atmosphere glove box (Mikrouna, H_2O < 0.1 ppm, O_2 < 0.1 ppm) with sodium foil as counter electrode, 1M $NaClO_4$ in a mixture of ethylene carbonate (EC) and diethyl carbonate (DEC) (1:1, v/v) as electrolyte, and glass fiber as separator. The galvanostatic charge/discharge test and galvanostatic intermittent titration technique (GITT) were conducted on a LANHE CT001 battery test system (Wuhan, China) with a potential range of 0.001-2.5 V (vs. Na/Na^+). The cyclic voltammetry (CV) and electrochemical impedance spectroscopy (EIS) tests were performed using a BioLogic VSP electrochemical workstation. The full cell was assembled using PFCC@PP as the anode and O3-$NaNi_{1/3}Fe_{1/3}Mn_{1/3}O_2$ (Shanghai Zijian Chemical Technology Co.) as the cathode with an N/P ratio of 1.1. The O3-$NaNi_{1/3}Fe_{1/3}Mn_{1/3}O_2$ cathode was prepared by dispersing the active material, Super P and PVDF with a mass ratio of 8:1:1 in N-methyl-2-pyrrolidone (NMP) solvent, and then coating the slurry onto aluminum foil current collector. The PFCC@PP and O3-$NaNi_{1/3}Fe_{1/3}Mn_{1/3}O_2$ electrodes were precycled in half-cell at a current rate of 0.1 C before assembling the full cell. The full cell was tested for charging and discharging within a voltage range of 0.5 - 4V.

Computational Methods

All theoretical calculations were performed via density functional theory (DFT) and the electronic structure of the materials were investigated in the Dmol^3 module of Materials Studio 2020. The PWC exchange correlation function was set to local gradient close to LDA and the dual digital basis DND 4.4 including the d polarization function were adopted to calculate the adsorption energies and differential charge densities. The electronic energy was considered to be self-consistent when the energy change was less than 10^{-5} eV. The geometry optimization was considered to be convergent when the energy change was less than 0.01 eV Å^{-1}. Horizontal graphene with a length and width of 12.3 × 9.9 Å was established and then compressed to form curved graphene at angles of 36°, 45° and 60° to simulate curved carbon layers in hard carbon, representing open and closed pore structures. The adsorption energy of Na (ΔE_{ads}) can be described by the following equation:

$$\triangle E_{ads} = E_{total} - E_{base} - E_{Na} \quad (1)$$

Where E_{total} is the total energy of the material with adsorbed Na atoms, and E_{base} and E_{Na} are the energy of the clean substrate and Na, respectively. The PWC exchange correlation function with local gradient close to LDA and the dual digital basis DND including the d polarization function were adopted to calculate the adsorption energies and differential charge densities. The isosurface values for the charge-difference figures is 0.005 Å^{-3}.

Models for SAXS data analysis

Small angle X-ray scattering (SAXS) technique stands as an important instrument for characterizing the microstructure of nanoporous materials. Porod's law is a fundamental formula in SAXS theory, which is mainly used to describe the asymptotic relationship between the scattering intensity and the scattering vector function [1]. For different samples, there are three different scattering characteristics of Porod curves, which are no deviation, negative deviation and positive deviation [2]. According to the test results, the materials prepared in this study belong to the positive deviation, and there was electron density micro-fluctuation in the range of 1-5 nm^{-1}. The expression

of Porod's law is:

$$ln[q^4 I(q)] = lnK + bq^2 \quad (2)$$

Where q is the scattering vector, $q = 4\pi \sin\theta / \lambda$, 2θ is the scattering angle, λ is the wavelength of the incident X-rays, I(q) is the scattering intensity, K is the Porod constant, and b is a constant related to the size of the regions with micro-fluctuations of electron density.

The specific surface area of the material was calculated from Porod's law as shown in equation:

$$S = \frac{\pi\varphi(1-\varphi)K}{Q\rho_P} \quad (3)$$

Where K is Porod constant, φ is the volume fraction of the dispersed phase, and for porous systems, φ is the porosity, which is usually derived from the absolute intensity of the density of the sample, and Q is the invariant, which is given by the formula:

$$Q = \int_0^\infty q^2 I(q) dq \quad (4)$$

For the calculation of Q, it is necessary to consider 0 to ∞, but in the practical measurement, the instrument is limited in its ability to measure extremely small or large q values and thus, can only be within a certain range. The test range for q was defined as $[q_1, q_2]$. When q is less than q_1, extrapolation of the linear part of the low q region according to Guinier approximation [3]. When q was greater than q_2, the scattering curve obeys the q^{-4} rule in that range according to Porod's law [4].

$$\varphi = 1 - \frac{\rho_p}{\rho_s} \quad (5)$$

$$\rho_s = \rho_g \times \frac{d_{002\ graphite}}{d_{002\ sample}} \quad (6)$$

The porosity of the material is calculated by the formulas [5], where ρ_p is the particle density and ρ_s is the structural density of the materials. For the calculation of ρ_s, where ρ_g is the theoretical density of graphite (2.26 g cm^{-3}), $d_{002\ graphite}$ and $d_{002\ sample}$ are the average interlayer spacing between graphite and sample. The value of $d_{002\ sample}$ was obtained by X-ray diffraction (XRD) pattern.

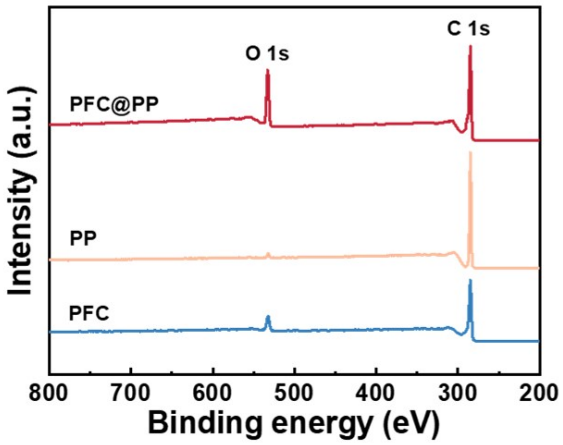

Fig. S1. XPS survey spectra of PFC, PP and PFC@PP.

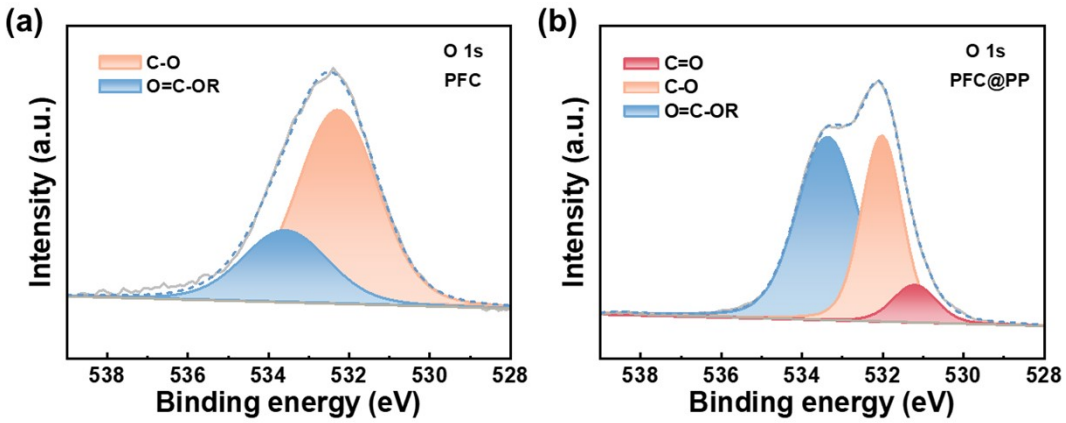

Fig. S2. High-resolution O 1s XPS spectra of (a) PFC and (b) PFC@PP.

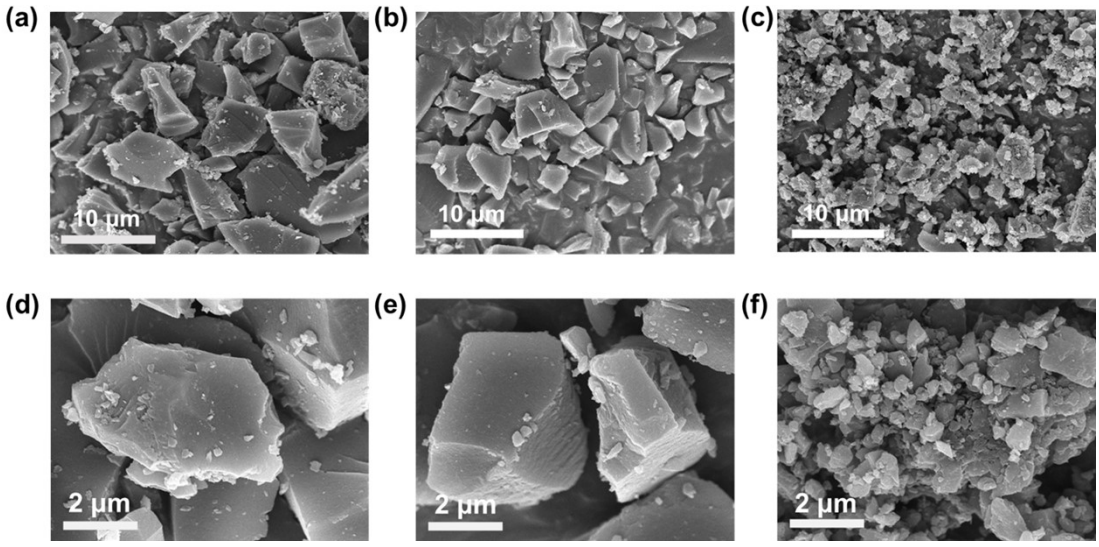

Fig. S3. SEM images of (a, d) PFC, (b, e) PFCC and (c, f) PFCC@PP.

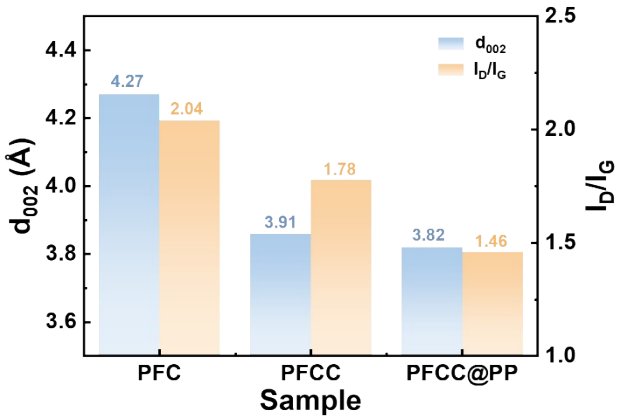

Fig. S4. Bar-graph depicting the variation of d_{002} and I_D/I_G of PFC, PFCC and

PFCC@PP.

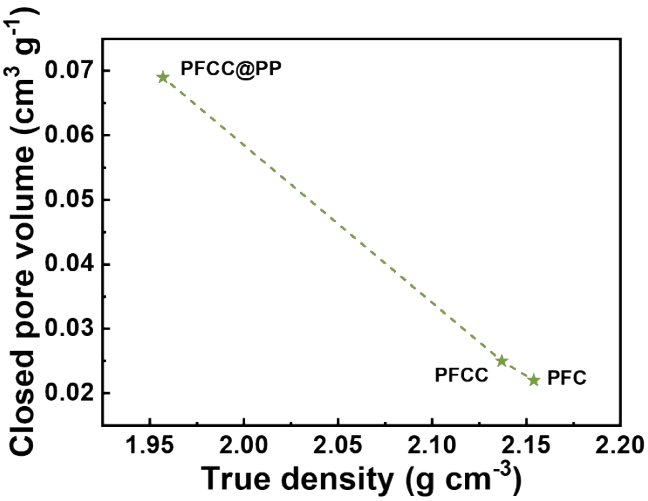

Fig. S5. True density of PFC, PFCC and PFCC@PP.

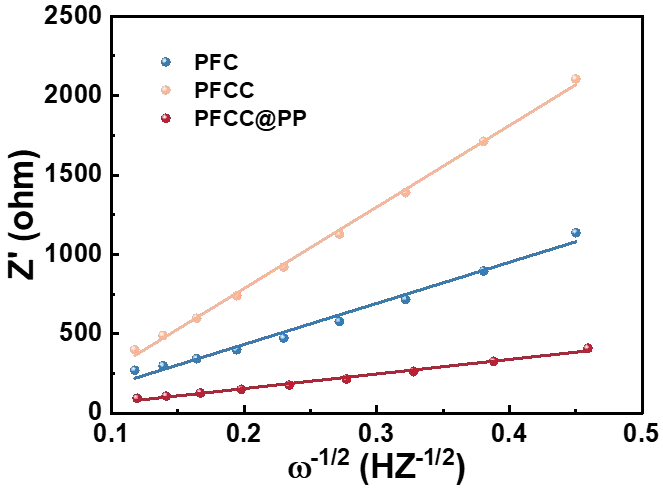

Fig. S6. Warburg profiles of PFC, PFCC and PFCC@PP.

$$D_{Na^+} = \frac{R^2T^2}{2A^2n^2F^4C^2\sigma^2} \quad (7)$$

$$Z' = R_s + R_{ct} + \sigma\omega^{-1/2} \quad (8)$$

Where R is the gas constant (8.314 J mol^{-1} K^{-1}), T is the absolute temperature (K), A is the electrode surface area, n is the number of electrons per molecule during the redox reaction, F is the Faraday constant (96500 C mol^{-1}), C is the Na^+ concentration, and σ

is the Warburg factor, which can be determined from a linear fit of Z' and $\omega^{-1/2}$ in the low-frequency region.

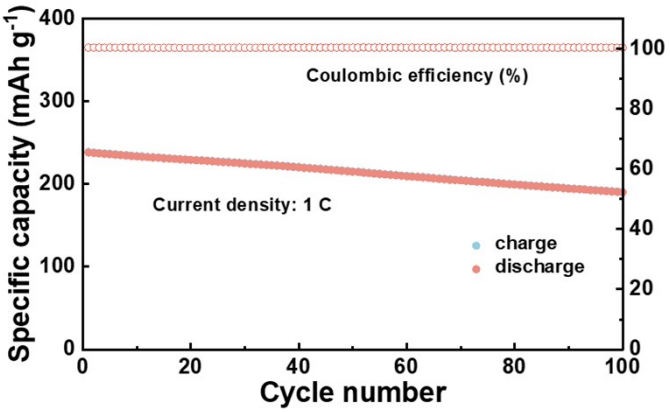

Fig. S7. Cycling performance at 1 C of the sodium-ion full cell.

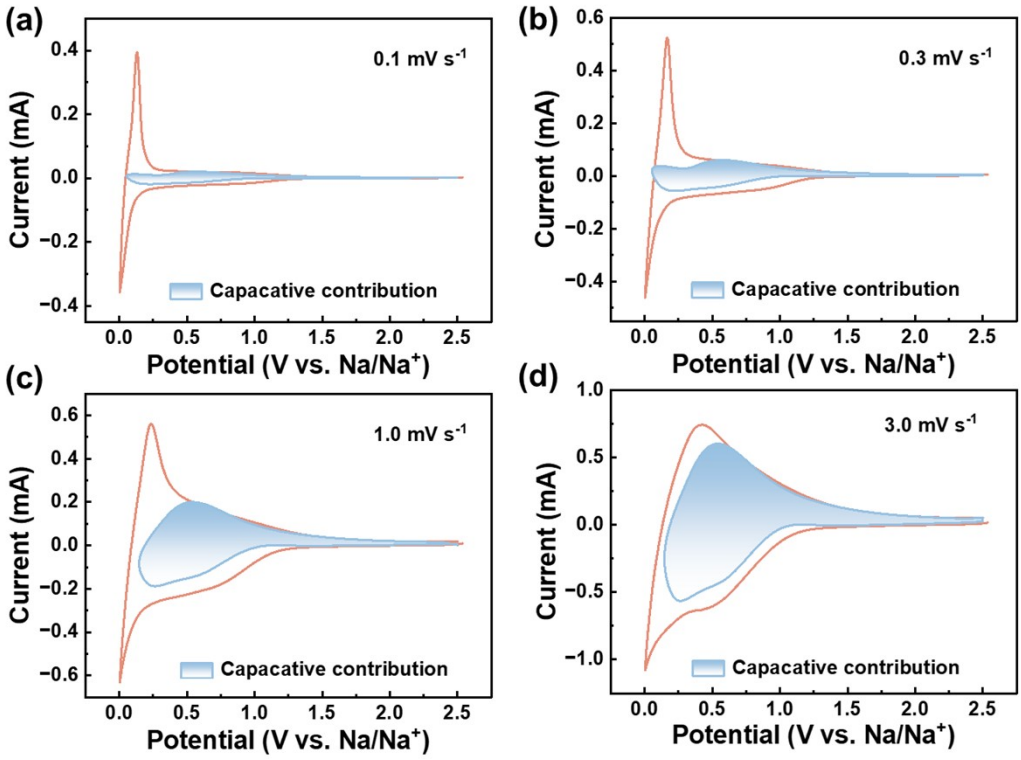

Fig. S8. CV curve of PFCC@PP electrode with calculated capacitive contribution at

(a) 0.1 mV s^{-1}, (b) 0.3mV s^{-1}, (c) 1.0 mV s^{-1} and (d) 3.0 mV s^{-1}.

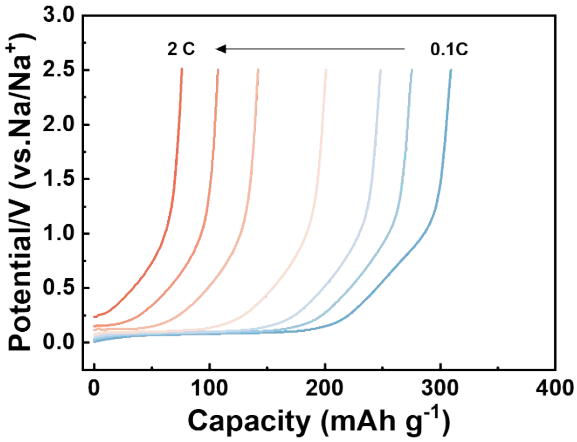

Fig. S9. Galvanostatic charge curves of PFCC@PP at different current rates.

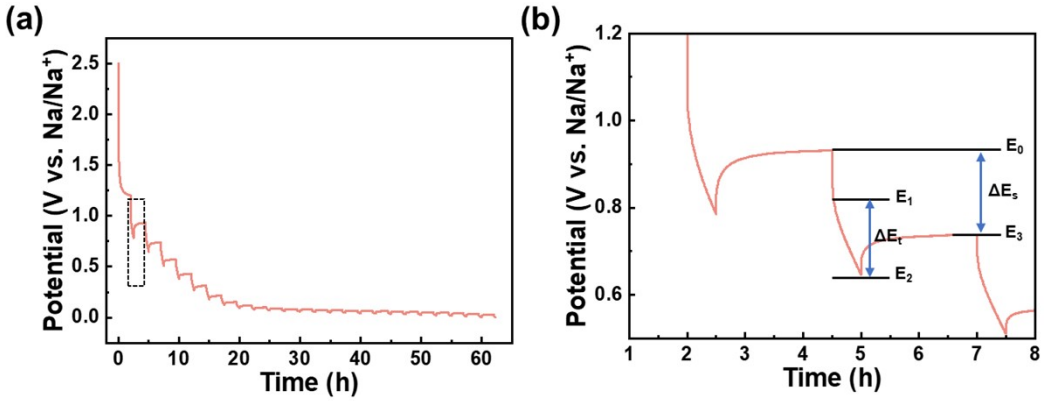

Fig. S10. (a) GITT plot of PFCC@PP and its (b) enlarged regions during discharge: ΔE_t is the voltage change of constant current discharging from E_1-E_2, and ΔE_s is the voltage change caused by the pulse from E_0-E_3.

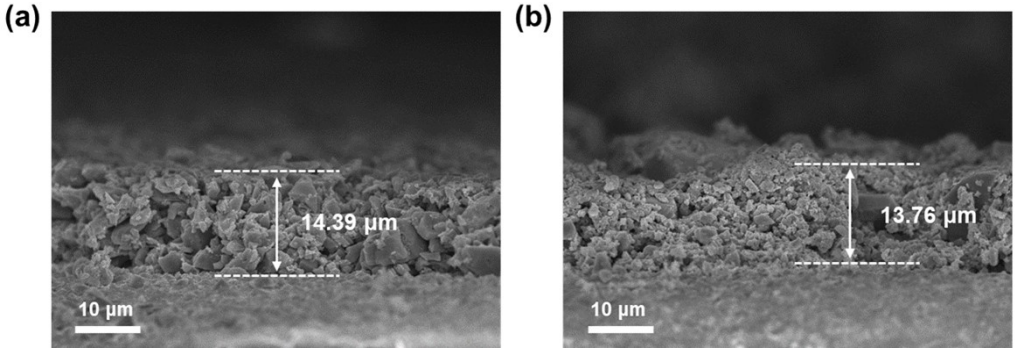

Fig. S11. The cross-sectional SEM images of (a) PFC and (b) PFCC@PP electrodes.

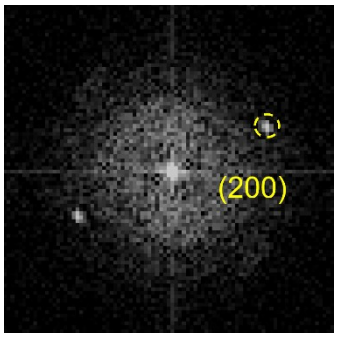

Fig. S12. The fast Fourier transform (FFT) of PFCC@PP.

Table S1 Element content from XPS survey of carbon samples.

Samples	C (at%)	O (at%)
PFC	89.2	10.8
PP	98.2	1.8
PFC@PP	79.0	21.0

Table S2 The structural characterization of the carbon samples.

Samples	d_{002} (nm)	I_D/I_G	$I_{D''}/I_G$	I_T/I_G
PFC	0.427	2.04	1.41	0.82
PFCC	0.391	1.78	1.01	0.63
PFCC@PP	0.382	1.46	0.78	0.55

Table S3 Pore structure parameter of PFC, PFCC and PFCC@PP.

Sample	S_{BET} ($m^2\ g^{-1}$)	V_t ($cm^3\ g^{-1}$)	S_{SAXS} ($m^2\ g^{-1}$)	$S_{Closed\ pore}$ ($m^2\ g^{-1}$)	ρ_{true} ($g\ cm^{-3}$)	$V_{Closed\ pore}$ ($cm^3\ g^{-1}$)
PFC	962.3	0.409	972	9.7	2.154	0.022
PFCC	949.6	0.402	1306	356.4	2.137	0.025
PFCC@PP	5.8	0.048	1100	1094.2	1.957	0.069

Table S4 Na-storage performance comparison of PFCC@PP with the reported carbons in the literatures.

	Carbon material	Reversible capacity (mAh g^{-1})	ICE (%)	Ref.
1	PO-SC-S	250	80	[6]
2	RH1600	276	53.1	[7]
3	FP-MP 5:2 1000	282	80	[8]
4	CUB-600	236.3	59.9	[9]
5	MCH	431	57	[10]
6	1400HCMNT	290	80	[11]
7	ChT-1100	326	71.2	[12]
8	POP3-1200	276.8	67.5	[13]
9	N-CNS-1050	304.7	79.5	[14]
10	N-AC-1200	282	/	[15]
11	WFC-1800	241.7	80.5	[16]
12	MoC@MCNs	289	81	[17]
13	HC-325-12	300.8	82.8	[18]
14	HHC	279.3	70.2	[19]
15	MPC-1100	318	71.2	[20]
	PFCC@PP	309.3	87.8	**This work**

Table S5. Fitted kinetic parameters of carbon electrode obtained by the equivalent electric circuit.

Samples	**R_{Ω} (Ω)**	**R_{ct} (Ω)**	**σ**	**D_{Na+} (cm^2 s^{-1})**
PFC	3.24	218.4	2679	2.24×10^{-10}
PFCC	4.69	200.4	4983	6.48×10^{-11}
PFCC@PP	3.16	66.7	877	2.09×10^{-9}

References:

1. D. Saurel; J. Segalini; M. Jauregui; A. Pendashteh; B. Daffos; P. Simon; M. Casas-Cabanas, *Energy Storage Mater.* 2019, **21**, 162-173.
2. Z.-H. Li, *Chin. Phys. C* 2013, **37**, 108002.
3. L. C. Li Denghua, Yang Yu, Wang Li'na, Cui Dongxia, Liu Zhe, Guo Yingying, *Materials Reports* 2021, **35**, 07077-07086.
4. L. Peng; B. Chen; Y. Zhao, *Constr. Build. Mater.* 2020, **262**,120863.
5. L. D. Cen Wei, Zhu Xiaoheng, Mao Bingquan, *Petrochemical Technology,* 2012, **41**, 97-102.
6. F. Xie; Y. Niu; Q. Zhang; Z. Guo; Z. Hu; Q. Zhou; Z. Xu; Y. Li; R. Yan; Y. Lu; M. M. Titirici; Y. S. Hu, *Angew. Chem. Int. Ed*., 2022, **61**, e202116394.
7. M. K. Rybarczyk; Y. Li; M. Qiao; Y.-S. Hu; M.-M. Titirici; M. Lieder, *J. Energy Chem.,* 2019, **29**, 17-22.
8. F. Xie; Z. Xu; A. C. S. Jensen; H. Au; Y. Lu; V. Araullo-Peters; A. J. Drew; Y. S. Hu; M. M. Titirici, *Adv. Funct. Mater.*, 2019, **29**, 1901072.
9. Y. Li; M. Kong; J. Hu; J. Zhou, *Adv. Energy Mater.*, 2020, **10**, 2000400.
10. L. Peng; H. Peng; L. Xu; B. Wang; K. Lan; T. Zhao; R. Che; W. Li; D. Zhao, *J. Am. Chem. Soc.*, 2022, **144**, 15754-15763.
11. Z.-E. Yu; Y. Lyu; Y. Wang; S. Xu; H. Cheng; X. Mu; J. Chu; R. Chen; Y. Liu; B. Guo, *Chem. Commun.*, 2020, **56**, 778-781.
12. S. Zhou; Z. Tang; Z. Pan; Y. Huang; L. Zhao; X. Zhang; D. Sun; Y. Tang; A. S. Dhmees; H. Wang, *SusMat*, 2022, **2**, 357-367.
13. L. Ji; Y. Zhao; L. Cao; Y. Li; C. Ma; X. Qi; Z. Shao, *J. Mater. Chem. A,* 2023, **11**, 26727-26741.
14. Y. Zhao; Z. Hu; C. Fan; P. Gao; R. Zhang; Z. Liu; J. Liu; J. Liu, *Small,* 2023, **19**, 2303296.
15. R. Li; B. Yang; A. Hu; B. Zhou; M. Liu; L. Yang; Z. Yan; Y. Fan; Y. Pan; J. Chen; T. Li; K. Li; J. Liu; J. Long, *Carbon,* 2023, **215**, 118489.
16. H. Wang; L. Shi; Z. Yang; J. Liu; Y. Xu; M. Song; J. Jiang; Q. Zhuang; Y. Chen;

Z. Ju, *Mater. Today Sustainability,* 2023, **24**, 100578.

17. Y. Liu; Y. Wan; J. Y. Zhang; X. Zhang; C. T. Hung; Z. Lv; W. Hua; Y. Wang; D. Chao; W. Li, *Small,* 2023, **19**, 2301203.
18. R. Xu; Z. Yi; M. Song; J. Chen; X. Wei; F. Su; L. Dai; G. Sun; F. Yang; L. Xie; C.-M. Chen, *Carbon,* 2023, **206**, 94-104.
19. Y. Qiu; G. Jiang; Y. Su; X. Zhang; Y. Du; X. Xu; Q. Ye; J. Zhang; M. Ban; F. Xu; H. Wang, *Carbon Energy,* 2024, e479.
20. J. L. Xia; D. Yan; L. P. Guo; X. L. Dong; W. C. Li; A. H. Lu, *Adv. Mater.,* 2020, **32**, 2000447.